

# Real and momentum space analysis of topological phases in 2D d-wave altermagnets

Manuel Calixto\*

*Department of Applied Mathematics and Institute Carlos I of Theoretical and Computational Physics, University of Granada, Granada 18071, Spain*

**Abstract:** Altermagnetism has recently emerged as a third fundamental branch of magnetism, combining the vanishing net magnetization of antiferromagnets with the high-momentum-dependent spin splitting of ferromagnets. This study provides a comprehensive real- and momentum-space analysis of topological phases in two-dimensional d-wave altermagnets. By employing a tight-binding Hamiltonian, we characterize the topological phase transition occurring at a critical intra-sublattice hopping strength ( $t_a^C$ ). We examine the emergence of Dirac nodal points and the resulting Berry curvature singularities, supported by a visual analysis of pseudospin texture winding. Crucially, we analyze spin splitting, effective altermagnetic strength, and investigate the transport implications of these phases, uncovering giant conductivity anisotropy and spin-dependent “steering” effects driven by group velocity distribution across the Fermi surface. Beyond bulk properties, we analyze the edge state topology in ribbon geometries through the lens of information-theoretic markers like fidelity-susceptibility and inverse participation ratio, offering an alternative to traditional Chern number calculations. Our results demonstrate that the hybridization of edge states in ultra-narrow nanoribbons opens a controllable energy gap —a feature we exploit to propose a novel topological altermagnetic field-effect transistor design where ballistic and spatially spin-polarized transport can be electrostatically gated. This work establishes a theoretical and information-theoretic framework for “edgetronics” in altermagnetic materials, paving the way for next-generation, high-speed spintronic and “spin-splitter” logic devices and architectures.

**Keywords:** Altermagnetism, Topological Phase Transition, d-wave symmetry, Spin-splitting, Edgetronics, Nanoribbon FET

## I. INTRODUCTION

For nearly a century, our understanding of magnetic order was built upon a fundamental binary: ferromagnetism (FM), characterized by parallel spin alignment and a net macroscopic magnetization, and antiferromagnetism (AFM), where antiparallel spins cancel each other out, resulting in a zero net magnetic moment. As noted in a recent editorial by Igor Mazin [1], altermagnetism (AM) has emerged as a “new punch line” (a third branch) in fundamental magnetism, disrupting this traditional dichotomy by introducing a third magnetic phase that combines the most desirable properties of both worlds.

The formalization of AM as a distinct phase was established in the seminal work by Šmejkal, Sinova, and Jungwirth [2]. This theoretical framework has mapped out an extensive “research landscape” [3], identifying numerous candidate materials across metals, insulators, and semiconductors. They demonstrated that certain collinear magnets possess a unique symmetry where opposite magnetic sublattices are connected by crystal rotations rather than the translations or inversions typical of conventional AFMs. This “nonrelativistic spin and crystal rotation symmetry” results in a vanishing net magnetization (like an AFM) but allows for large, momentum-dependent spin splitting in the electronic bands (like a FM), even without considering spin-orbit coupling.

Indeed, the most striking signature of an AM is the Kramers spin degeneracy lifting in momentum space, experimentally confirmed in [4]. Traditional AFMs maintain degenerate spin-up and spin-down bands due to the combination of time-reversal and inversion symmetry, whereas AMs break this degeneracy. In colloquial terms, spin polarization is the “secret sauce”. The significance of AM lies in its potential for spintronics. The spin polarization in AMs is not a weak effect because it is protected by the crystal lattice symmetry. Spin polarization allows the material to behave like an FM in transport experiments while acting like an AFM in terms of magnetic stability. In other words, AMs combine the best of both worlds. Usually, spin polarization is a trade-off. To get spin-polarized currents, you use Ferromagnets (FM), but they produce stray magnetic fields that interfere with neighboring devices and are limited by slow dynamics. We use AFMs to avoid stray fields and low dynamics, but they usually have degenerate (non-polarized) bands, making them harder to read, manipulate, and use for electronic signals. AMs break this trade-off. Since the spin polarization in an AM is directionally dependent (e.g., d-wave, g-wave or p-wave symmetries [5] describing the shape of the spin splitting in momentum space), an AM acts as a “spin filter” that depends on the electron’s velocity.

---

\* [calixto@ugr.es](mailto:calixto@ugr.es)

We will show later in Section IV how, in a  $d_{x^2-y^2}$ -wave AM, electrons traveling along the  $x$ -axis could have mostly spin up, while those along the  $y$ -axis could have mostly spin down. In short, AMs offer the high-speed, robust nature of AFMs while providing the spin-polarized currents necessary for device functionality.

In terms of experimental observation, two prototypical materials have provided the “smoking gun” evidence for this exotic topological phase of nature. First, research on MnTe using angle-resolved photoemission spectroscopy, provided direct experimental confirmation of AM band splitting [4, 6]. Second, in the metallic regime, ruthenium dioxide ( $\text{RuO}_2$ ) has served as a critical test bench. Early experimental evidence for AM in  $\text{RuO}_2$  came from the observation of a “Crystal Hall Effect” [7, 8]. The list of references is enormous, with considerable growth in recent years. Prospects in giant magnetoresistance is promising because AMs allow the creation of magnetic tunnel junctions due to massive changes in resistance depending on the relative orientation of two AM layers. AMs may also improve the efficiency of Spin-Orbit Torque Magnetic Random-Access Memories (SOT-MRAM). While conventional SOT-MRAM relies on the spin-Hall effect in heavy metals [9–11], AMs offer a newly discovered mechanism: the Spin-Splitter Torque (SST) [12]. Recent experiments in  $\text{RuO}_2$  have demonstrated that this intrinsic torque is highly efficient [13], paving the way for single-layer, low-power, ultra-fast memory devices that combine the readout capabilities of FMs with the Terahertz dynamics of AFM [14].

This study takes a theoretical approach while keeping an eye on possible physical applications. Our goal is to delve deeper into the internal structure of the spectrum and wave functions to better understand the nature of the topological phase transition (TPT) in AMs. The article also aims to be instructive, providing sufficient detail to be as self-contained as possible, so that it can be read by an audience that is not necessarily an expert in the subject. The reason for doing so is that, from time to time, we follow an information-theory perspective, which may not be the usual approach for readers coming from condensed matter physics, and vice versa. The article is organized as follows. In Section II we introduce the model, discuss the real-space crystal structure and the momentum-space band structure, as well as the corresponding tight-binding Hamiltonians and their diagonalization. Section III is dedicated to the discussion of nodal/Dirac points and a Berry phase analysis to visualize and highlight the TPT that occurs in AMs for a critical value of the intra-sublattice AM hopping strength  $t_a$ . In Section IV we study the spin splitting and effective altermagnetic strength, together with the group velocity distribution across the Fermi surface, and conductivity anisotropy profiles. The information-theoretic concept of fidelity-susceptibility is introduced in Section V to characterize TPTs as an alternative to traditional topological quantum (Chern, Pontryagin, winding, etc) numbers. This Section is also devoted to a real-space crystal structure analysis, together with a calculation and interpretation of the spatial segregation texture (or chirality) and global and local density of states in line with the spin-splitting and conductivity anisotropy pictures. In this Section we also study the appearance of a hybridization gap in finite nanoribbons; this robust and controllable gap can be used to design a novel altermagnetic topological field-effect transistor (FET), where ballistic spin transport can be electrostatically gated. Another information-theoretic concept, called inverse participation ratio (IPR) and linked to the Rényi entropy of order two, is introduced in Section VI to analyze the edge state structure and localization in an infinite strip geometry. Finally, Section VII is left for conclusions and future directions.

## II. d-WAVE ALTERMAGNET LATTICE STRUCTURES AND HAMILTONIAN MODELS

In Figure 1 we represent the real-space crystal structure of 2D lattice d-wave altermagnets of type  $d_{x^2-y^2}$  and  $d_{xy}$ . The sublattice  $A$  (blue) and sublattice  $B$  (red) possess opposite magnetic moments  $-m$  and  $m$  represented by down  $\downarrow$  and up  $\uparrow$  white arrows. The sublattices  $A$  and  $B$  then act as an antiferromagnet, exerting opposite exchange fields on the spin  $s = \pm 1$  itinerant electrons. According to Hund’s rule, an electron spin aligns with the local magnetic moment to lower its energy. In the Hamiltonian, this results in a staggered exchange potential energy of  $+sJ$  and  $-sJ$  for  $A$  and  $B$  type sites, respectively, with  $J$  the energy splitting (exchange field strength). The gray lines represent nearest-neighbor (NN) hopping  $t$  between  $A$  and  $B$  sites, while the yellow and green lines represent the characteristic altermagnetic next-nearest-neighbor (NNN) hopping amplitudes  $+t_a$  and  $-t_a$ , respectively. Let us denote by  $\mathbf{k} = (k_x, k_y)$  the wave vector and by  $\boldsymbol{\tau} = (\tau_x, \tau_y, \tau_z)$  the Pauli matrices acting on the lattice (pseudo-spin) sector ( $A, B$ ). The Hamiltonian for spin  $s$  electrons in momentum space adopts the form  $H_s(\mathbf{k}) = \mathbf{d}_s(\mathbf{k}) \cdot \boldsymbol{\tau}$ , where the three-vector  $\mathbf{d}_s = (d_x^s, d_y^s, d_z^s)$  plays the role of an “effective Zeeman field in pseudospin space”. The NN interaction contributes to the Hamiltonian  $H_s(\mathbf{k})$  through a  $d_x^s \tau_x + d_y^s \tau_y$  term with

$$d_x^s(\mathbf{k}) - i d_y^s(\mathbf{k}) = t \sum_{\delta} e^{i \mathbf{k} \cdot \boldsymbol{\delta}}, \quad (1)$$

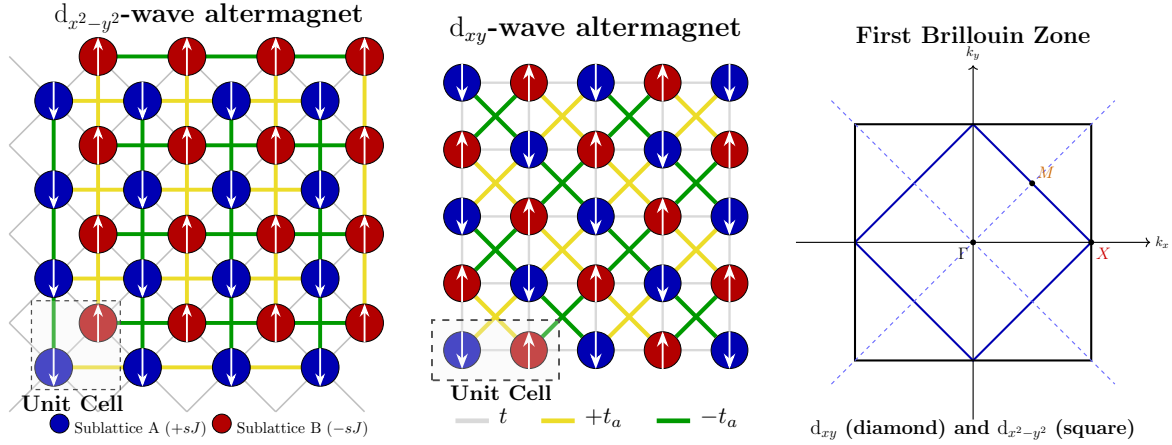


FIG. 1. Real-space representation of 2D  $d_{x^2-y^2}$ -wave and  $d_{xy}$ -wave AM lattices and their BZs.

where  $\delta$  denote the NN vector hoppings. Similarly, the NNN AM interaction and the exchange potential energy  $sJ$  both contribute to the  $d_z^s \tau_z$  Hamiltonian part as follows

$$d_z^s(\mathbf{k}) = sJ + t_a \sum_{\delta'} \text{sgn}(\delta') e^{i\mathbf{k} \cdot \delta'}, \quad (2)$$

where  $\delta'$  denote the NNN vector hoppings and  $\text{sgn}(\delta') = \pm 1$  assigns their corresponding sign to account for the AM symmetry.

For a  $d_{x^2-y^2}$ -wave AM we have four NN hoppings

$$\delta = a(\pm 1/2, \pm 1/2) \rightarrow d_y^s = 0, d_x^s(\mathbf{k}) = 4t \cos\left(\frac{k_x}{2}\right) \cos\left(\frac{k_y}{2}\right). \quad (3)$$

We shall set the lattice constant to  $a = 1$  nm for convenience. Note that, since  $d_y^s = 0$ , the Hamiltonian  $H_s(\mathbf{k})$  is real and PT symmetric. This can be inconvenient for later Berry curvature analysis or for numerical/computational calculations in real space. Therefore, we also use the unitarily/gauge equivalent configuration

$$\delta = (0, 0), (-1, 0), (0, -1), (-1, -1) \rightarrow d_x^s(\mathbf{k}) - id_y^s(\mathbf{k}) = 4t \cos\left(\frac{k_x}{2}\right) \cos\left(\frac{k_y}{2}\right) e^{-i\phi(\mathbf{k})}, \quad (4)$$

where  $\phi(\mathbf{k}) = (k_x + k_y)/2$  is a phase that does not change the Hamiltonian spectrum. Similarly, the  $d_z^s \tau_z$  Hamiltonian part reduces to

$$d_z^s(\mathbf{k}) = sJ + t_a(e^{-ik_x} + e^{ik_x} - e^{-ik_y} - e^{ik_y}) = sJ + 2t_a(\cos(k_x) - \cos(k_y)). \quad (5)$$

Analogously, for  $d_{xy}$ -wave AMs we have

$$d_x^s(\mathbf{k}) = 2t(\cos(k_x) + \cos(k_y)), \quad d_z^s(\mathbf{k}) = sJ - 4t_a \sin(k_x) \sin(k_y). \quad (6)$$

The  $d_{x^2-y^2}$  and  $d_{xy}$  nomenclature makes reference to the low momentum  $d_z^s$  expansions  $d_z^s \sim k_x^2 - k_y^2$  and  $d_z^s \sim k_x k_y$ , respectively, imitating two of the five d orbitals  $\{d_{x^2-y^2}, d_{xy}, d_{xz}, d_{zx}, d_{z2}\}$  (or electronic configurations) for the azimuthal quantum number  $l = 2$  in the atom (see later in Figure 5 for conductivity polar plots).

Spin-orbit couplings usually contribute to the  $d_y^s \tau_y$  Hamiltonian part. The interesting consequences of spin-orbit coupling are left for future studies.

The Hamiltonian  $H_s = \mathbf{d}_s \cdot \boldsymbol{\tau}$  eigenvalues [conduction (+) and valence (-) bands] and eigenstates (two-spinors) are simply as follows

$$E_s^{\pm} = \pm |\mathbf{d}_s|, \quad |\psi_{\pm}^s\rangle = \begin{pmatrix} \psi_A^s \\ \psi_B^s \end{pmatrix}_{\pm} = \begin{pmatrix} \frac{d_x^s \pm i d_y^s}{\sqrt{d_x^s + i d_y^s}} \\ 1 \end{pmatrix}. \quad (7)$$

Unless otherwise stated, we shall restrict ourselves to the  $d_{x^2-y^2}$ -wave AM case and comment on the essential differences with the  $d_{xy}$ -wave AM case when appropriate. The valence band minimum and the conduction band maximum energies are attained at the  $\Gamma$  point  $\mathbf{k} = (0, 0)$  with values

$$E_s^\pm(\Gamma) = \pm \sqrt{J^2 s^2 + 16t^2}. \quad (8)$$

We shall fix  $J = 1 = t$  meV for numerical calculations along the paper, which gives  $E_s^\pm(0, 0) \simeq 4.12$  meV.

In the next sections, we analyze the structure and evolution of the valence band maximum (VBM) and conduction band minimum (CBM) Hamiltonian eigenstates as a function of the AM hopping  $t_a$ . For  $t_a \leq J/4$  (low AM hopping strength compared to exchange field strength), the energies attained at  $\mathbf{k} = (0, \pm\pi)$  for  $s = -1$  and at  $\mathbf{k} = (\pm\pi, 0)$  for  $s = 1$  give a band gap of:

$$E_g = E_{\text{CBM}} - E_{\text{VBM}} = 2(J - 4t_a), \quad t_a \leq J/4. \quad (9)$$

The topological AM structure around the critical point

$$t_a^C = J/4 \quad (10)$$

is analyzed in the next section.

### III. NODAL/DIRAC POINTS AND BERRY PHASE ANALYSIS

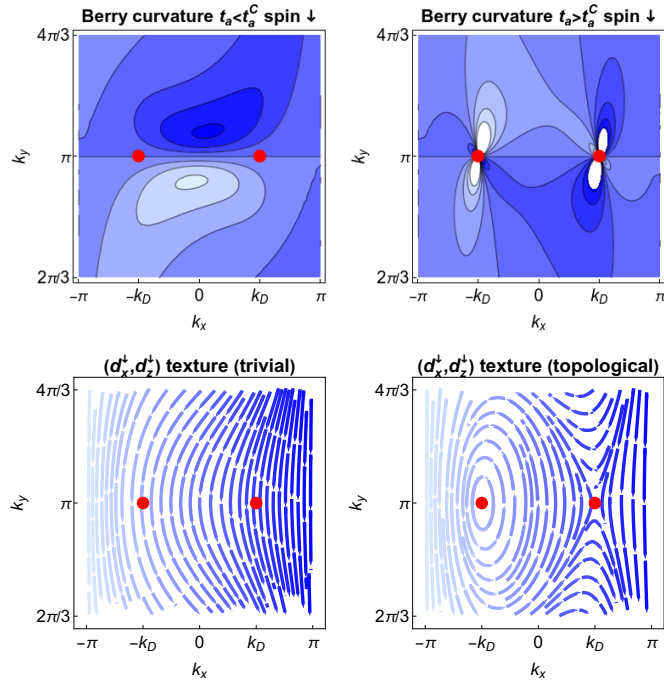


FIG. 2. Berry curvature (top row) and pseudo-spin (pseudo-Zeeman field) texture (bottom row) as a function of  $\mathbf{k} = (k_x, k_y)$  for spin  $s = -1$  in the trivial phase  $t_a < J/4$  (left) and the topological phase  $t_a > J/4$  (right). Dirac points  $\mathbf{k}_D = (\pm k_D, \pi)$  for  $t_a > J/4$  are marked with filled red dots in both contour and vector plots.

The energy gap  $E_g = 2|d_s|$  closes only when  $d_x^s = 0 = d_z^s$ . The off-diagonal hopping term is zero when

$$d_x^s(\mathbf{k}) = 4t \cos(k_x/2) \cos(k_y/2) = 0 \Rightarrow k_x = \pm\pi \quad \text{or} \quad k_y = \pm\pi, \quad (11)$$

which defines the nodal lines [for a  $d_{xy}$ -wave AM, the nodal lines are the diagonals  $k_x = \pm k_y$  marked by dashed blue lines in the BZ of Figure 1]. For  $k_y = \pm\pi$ ,

$$d_z^s(\mathbf{k}) = sJ + 2t_a(\cos(k_x) - \cos(\pi)) = 0 \Rightarrow k_x = \pm \arccos\left(\frac{J}{2t_a} - 1\right) \equiv \pm k_D, \quad (12)$$

which defines the Dirac points  $\mathbf{k}_D^\pm = (\pm k_D, -\pi)$  [and equivalent  $(\pm k_D, \pi)$ ] for  $t_a > t_a^C$  and  $s = -1$ , with  $t_a^C$  the critical point already defined in (10). We assume that  $J, t_a \geq 0$ . For  $k_x = \pm\pi$  and  $s = 1$ , the Dirac points are  $\mathbf{k}'_D^\pm = (-\pi, \pm k_D)$  [and the equivalent  $(\pi, \pm k_D)$ ]. Defining the Fermi velocities

$$v_1 = \sqrt{(4t_a - J)\bar{J}/\hbar}, \quad v_2 = t\sqrt{J/t_a}/\hbar, \quad t_a > t_a^C, \quad (13)$$

the first-order energy dispersion expansions around the Dirac points  $\mathbf{k}_D^\pm$  and  $\mathbf{k}'_D^\pm$  are

$$E_{-1}^\pm(q_x, q_y) = \pm\hbar\sqrt{v_1^2 q_x^2 + v_2^2 q_y^2}, \quad \text{and} \quad E_1^\pm(q'_x, q'_y) = \pm\hbar\sqrt{v_2^2 q'_x + v_1^2 q'_y}, \quad (14)$$

with  $\mathbf{q} = \mathbf{k} - \mathbf{k}_D^\pm$  and  $\mathbf{q}' = \mathbf{k} - \mathbf{k}'_D^\pm$ . The anisotropy in the Fermi velocity leads to directional dependence in the transport, which will be discussed in Section IV.

We want to ensure that a TPT from a band/trivial insulator (BI) to a topological insulator/metal (TI) phase exists when crossing the critical point  $t_a^C$ . For this purpose, the Berry phase  $\oint_\gamma \mathbf{A} \cdot d\vec{\mathbf{k}}$  is analyzed for a given loop  $\gamma$ , with

$$\mathbf{A}_\pm^s(\mathbf{k}) = -i\langle\psi_\pm^s(\mathbf{k})|\nabla_{\mathbf{k}}|\psi_\pm^s(\mathbf{k})\rangle$$

the Berry potential for Hamiltonian eigenstates (7) properly normalized. For  $d_y^s = 0$  the system possesses  $PT$  symmetry and we have real eigenvectors  $|\psi_\pm^s(\mathbf{k})\rangle$  which give zero Berry potential and curvature, except for singularities at the nodal points where the projection is undefined; therefore, for this analysis we resort to the complex (gauge equivalent) version (4). In Figure 2 we represent the Berry curvature

$$B_\pm^s(\mathbf{k}) = \frac{\partial(A_\pm^s)_y}{\partial k_x} - \frac{\partial(A_\pm^s)_x}{\partial k_y} = \pm\frac{1}{2} \left( \frac{\partial\hat{\mathbf{d}}_s(\mathbf{k})}{\partial k_x} \times \frac{\partial\hat{\mathbf{d}}_s(\mathbf{k})}{\partial k_y} \right) \cdot \hat{\mathbf{d}}_s(\mathbf{k})$$

( $\hat{\mathbf{d}}_s = \mathbf{d}_s/|\mathbf{d}_s|$ ) for  $s = -1$  and conduction band (+) in the insulating ( $t_a < t_a^C$ ) and topological ( $t_a > t_a^C$ ) phases. In the gapped phase, the Berry curvature extends into the Brillouin zone with low absolute values  $|B_+^{-1}(\mathbf{k})| \ll 1$  and a zero Chern number [basically, the Berry phase for the FBZ border  $\gamma$ , or the integral of  $B_\pm^s(\mathbf{k})$  over the FBZ]. In the topological insulator phase, the Berry curvature displays a Dirac delta-like distribution that is highly localized at the Dirac points (indicated by thick red dots in Figure 2), giving a non-zero ( $\pi$ ) Chern number. Because the delta function behavior introduces numerical instabilities, we also propose to visualize the TPT through the winding of the pseudospin texture (the three-vector  $\mathbf{d}$ ) around the nodal points. In Figure 2 we also plot the vector field  $(d_x^s, d_y^s)$  texture (for the real Hamiltonian) in the BI and TI phases. For  $t_a < t_a^C$ ,  $\mathbf{d}$ -streams flow smoothly without swirls (zero winding number). For  $t_a > t_a^C$ , one sees two distinct vortices centered at the Dirac (red) points. This swirl is a visual representation of the topological charge. In you walk around a vortex, the vector rotates by  $360^\circ$ , which corresponds to a Berry phase of  $\pi$  for the wavefunction (spinor). We will provide a complementary (information-theoretic) characterization of the TPT in Section V A inside the real-space (versus momentum-space) picture of altermagnetism.

In Figure 3 we represent the Hamiltonian spectrum  $E_s^\pm(\mathbf{k})$  as a function of  $k_x$  (for several values of  $k_y$ ) and for the spin-up (red) and spin-down (blue) electrons in the TI phase ( $t_a > t_a^C$ ). The Hamiltonian spectrum is equivalent under the combined exchange of  $k_x \leftrightarrow k_y$  and  $\uparrow \leftrightarrow \downarrow$  (i.e., blue  $\leftrightarrow$  red). Edge states develop above the critical point  $t_a^C$ , closing the gap at the Dirac points  $\pm k_D$ . The thick dashed curves correspond to  $E_\downarrow^\pm(k_x, \pi)$  (blue) and  $E_\uparrow^\pm(k_x, k_D)$  (red). A crossing of both curves occurs at

$$k_E = \text{arcsec} \left( \frac{2(t^2 + 2t_a^2)}{Jt_a - 2t^2 - 4t_a^2} \right), \quad (15)$$

( $E$  makes reference to “edge”) where spin-up and spin-down edge Hamiltonian eigenstates degenerate. Dirac ( $k_D$ ) and edge crossing ( $k_E$ ) points are marked by vertical grid lines in Figure 3 (left panel).

Let us delve deeper into the structure of the AM Hamiltonian spectrum.

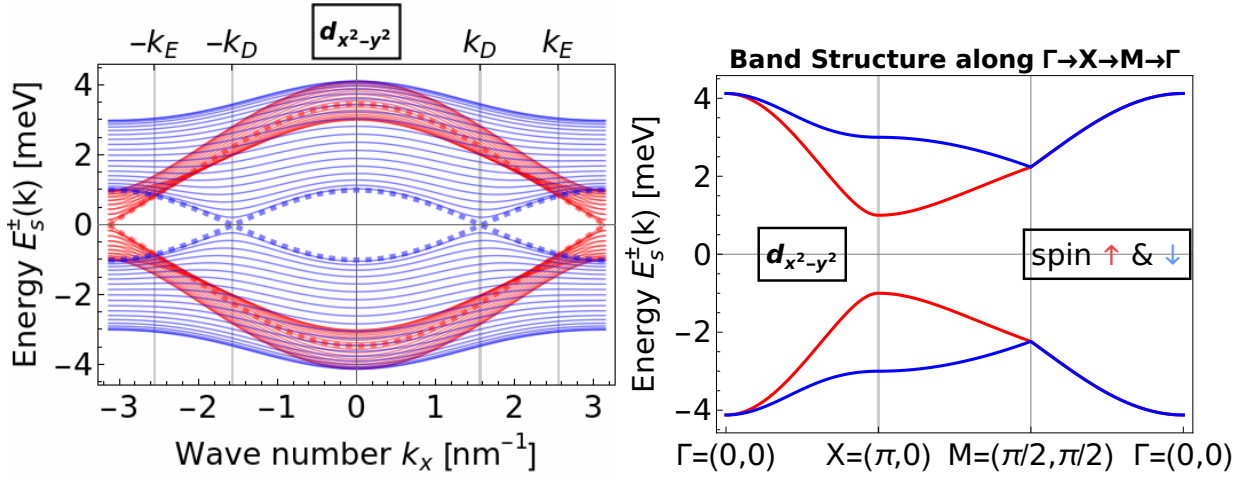


FIG. 3. Left: Energy dispersion as a function of  $k_x$  for 20 values of  $k_y$ . Right: Spin splitting along the trajectory  $\Gamma \rightarrow X \rightarrow M \rightarrow \Gamma$  in BZ. Hamiltonian parameters  $J = 1 = t, t_a = 0.5 > t_a^c = J/4$

#### IV. SPIN-SPLITTING, EFFECTIVE ALTERMAGNETIC STRENGTH AND ANISOTROPY OF CONDUCTIVITY.

##### A. Spin splitting and effective altermagnetic strength

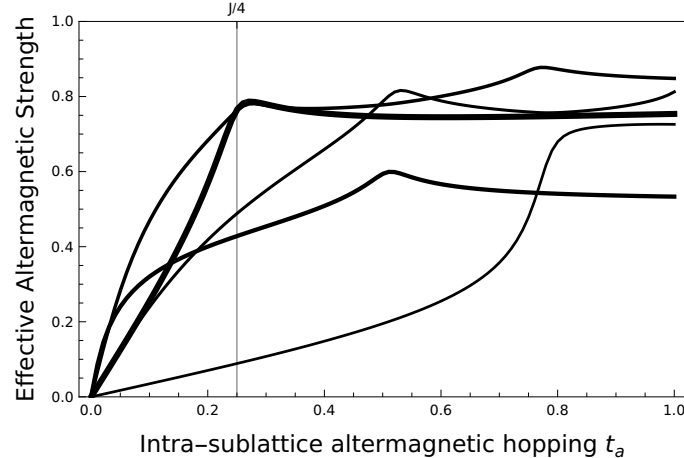


FIG. 4.  $P_{\text{eff}}$  versus  $t_a$  for the Fermi energies  $E_F = n\sqrt{J^2 + 16t_a^2}/4, n = 0, 1, 2, 3, 4$  (from thickest to thinnest curves). The critical point  $t_a^c = J/4$  is marked with a vertical gridline. Hamiltonian parameters:  $J = 1 = t$  and broadening  $\eta = 0.1$  meV.

In a conventional FM, spin polarization is a global property: you have more  $\uparrow$  electrons than  $\downarrow$  electrons throughout the entire crystal. In an AM, the global polarization is zero, but the local polarization in momentum space is high. The spin splitting at a fixed momentum  $\mathbf{k}$  is defined as follows

$$\Delta E(\mathbf{k}) = |E_\uparrow(\mathbf{k}) - E_\downarrow(\mathbf{k})|. \quad (16)$$

For our specific  $d_{x^2-y^2}$ -wave AM, and for small  $t_a$  and  $J$ , this splitting is dominated by the AM term  $|d_z^s(\mathbf{k})|$  in (5), which attains the values  $|d_z^s(0, \pi)| = |sJ + 4t_a|$  and  $|d_z^s(\pi, 0)| = |sJ - 4t_a|$  at points  $X = (\pi, 0)$  and  $Y = (0, \pi)$  of the FBZ. The spin splitting at those points is maximum with the value

$$\Delta E(X) = ||J - 4t_a| - |J + 4t_a|| = \begin{cases} 8t_a, & \text{if } t_a < t_a^c, \\ 2J, & \text{if } t_a \geq t_a^c. \end{cases}, \quad (17)$$

which exhibits a “clip”, or saturated ramp, behavior as a function of  $t_a$ . For the  $d_{xy}$ -wave AM, maximum spin splitting is attained at  $M = (\pi/2, \pi/2)$ . The variation of spin splitting along the closed path  $\Gamma \rightarrow X \rightarrow M \rightarrow \Gamma$ , drawn in the FBZ of Figure 1, can be appreciated from the band structure in Figure 3 (right panel) along this path.

Similarly, the local spin polarization at the Fermi level  $E_F$  is defined as follows

$$P(\mathbf{k}) = \frac{A_{\uparrow}(\mathbf{k}, E_F) - A_{\downarrow}(\mathbf{k}, E_F)}{A_{\uparrow}(\mathbf{k}, E_F) + A_{\downarrow}(\mathbf{k}, E_F)} \quad (18)$$

with

$$A_s(\mathbf{k}, E_F) \approx \delta_{\eta}(E_F - E_s(\mathbf{k})) \quad (19)$$

the spectral weight function (density of states), with the Dirac delta often approximated by the Lorenzian  $\delta_{\eta}(x) = (\eta/\pi)/(x^2 + \eta^2)$  for a given broadening  $\eta$  defining the Fermi Surface (FS) thickness. FS is defined by the set of points in  $\mathbf{k}$ -space where the energy equals  $E_F$ .

Because of the AM symmetry, for every point  $\mathbf{k}$  with positive polarization, there is a point  $\mathbf{k}'$  (rotated by  $90^\circ$ ) with equal and opposite negative polarization. Therefore, the total/net polarization

$$P_{\text{net}} = \frac{1}{4\pi^2} \int_{BZ} P(\mathbf{k}) d^2\mathbf{k} \quad (20)$$

is zero. This is the reason why an altermagnet shows no macroscopic magnetization and produces no stray fields. Therefore, to measure the “strength” of the AM effect, we take the absolute value of the local polarization. This indicates the average degree of spin-purity of electron if we select a random direction  $\mathbf{k}$  in momentum space. The Effective Polarization

$$P_{\text{eff}} = \frac{1}{4\pi^2} \int_{BZ} |P(\mathbf{k})| d^2\mathbf{k} \quad (21)$$

quantifies how much “usable” spin is available for transport by measuring the magnitude of the spin-splitting  $t_a$ , regardless of its sign. In Figure 4 we represent  $P_{\text{eff}}$  as a function of the AM strength  $t_a$  for five equi-spaced values of  $E_F \in [0, E_{\text{max}}]$  (from thickest to thinnest curves) with  $E_{\text{max}}$  the conduction band maximum energy in (8). The behavior of the dependence of  $P_{\text{eff}}$  on  $t_a$  resembles that of the saturated ramp giving the maximum spin splitting  $\Delta E(X)$  in (17). For  $t_a < J/4$  (band insulator phase), the effective polarization is an increasing function of  $t_a$ . For  $t_a > J/4$  (topological insulator phase), the effective polarization attains values near 0.8, except for Fermi energies close to  $E_{\text{max}}$  where the density of states is lower.

$P_{\text{eff}}$  matters for technology. A value of  $P_{\text{eff}} = 0.8$  means that, on average, an electron at the FS is 80% “spin-pure”. In the next section we will see that AM materials come with a privileged direction for electric conduction. Because polarization is tied to  $\mathbf{k}$ , we can “filter” electrons. If we created a device that only allowed transport along the maximum spin-splitting (nodal) directions  $X$  and  $Y$  (or the diagonals for  $d_{xy}$ ), the operational polarization would approach 100%, even though the material is globally “antiferromagnetic”.

Next we analyze the group velocity distribution across the FS and giant AM conductivity anisotropy.

## B. Group velocity distribution across the Fermi surface and anisotropy of conductivity

To understand why AMs generate spin currents, we have to look at the group velocity

$$\mathbf{v}_s(\mathbf{k}) = \frac{1}{\hbar} \nabla_{\mathbf{k}} E_s(\mathbf{k}). \quad (22)$$

This vector indicates the direction and speed at which an electron with momentum  $\mathbf{k}$  and spin  $s$  actually moves through the crystal.

To visualize which spin dominates transport, we look at the FS. In an AM, the FS for spin-up and spin-down electrons will have different shapes, even though they enclose the same total area. This “shape anisotropy” is why spin-polarized effects can be obtained without a net magnetic moment.

In Figure 5, we draw  $E_s^{\pm}(\mathbf{k}) = E_F^{\pm} = \pm 2$  meV FS contours for  $J = 1 = t, t_a = 0.2$  meV. FSs appear as two concentric-like loops, but with a twist for spin up (red) and down (blue), for valence (-) and conduction (+) electrons. The blue loops are stretched along the  $X$  direction, while the red loops are stretched along the  $Y$  direction. The two loops cross at the diagonals  $k_x = \pm k_y$  of the BZ, where the AM term  $(\cos k_x - \cos k_y)$  vanishes, causing spin degeneration. This visualization explains the anomalous Hall effect in AMs. Let us analyze the transport implications.

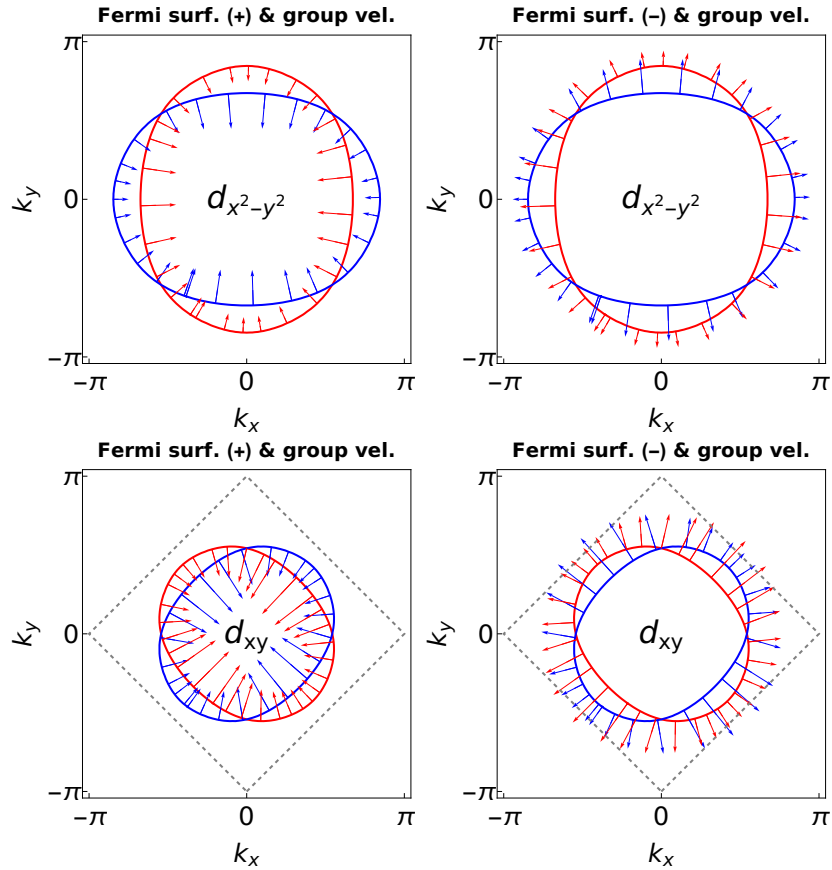


FIG. 5. Group velocity distribution across the FS ( $E_F = \pm 2$  meV), for conduction (+) and valence (−) bands and spin up (red) and down (blue)). Hamiltonian parameters:  $J = 1 = t, t_a = 0.2$  meV

In Figure 5 we also represent the group velocity  $\mathbf{v}_s(\mathbf{k})$  (in arbitrary units) for spin-up (red arrows) and spin-down (blue arrows) valence (−) and conduction (+) electrons at the FS. The group velocities turn out to be highly directional (anisotropic), displaying a “steering” effect. Since the electron velocity  $\mathbf{v}_s(\mathbf{k})$  is the slope of  $E_s(\mathbf{k})$ , the preference comes from how the altermagnetic energy term modifies the electron’s speed (group velocity) in different directions. For spin  $\uparrow$ , the altermagnetic term adds to the kinetic energy slope along the  $X$  direction, the effective mass drops, and the electron becomes fast. Along  $Y$ , the AM term subtracts from the slope, the effective mass increases and the electron becomes slow. For spin  $\downarrow$  the signs flip: electrons are slow along  $X$  and fast along  $Y$ . For  $d_{xy}$ -wave AM, the fast nodal lines are the diagonals:  $X = Y$  for spin  $\uparrow$  and  $X = -Y$  for spin  $\downarrow$ . This AM effect creates a spin-polarized current (longitudinal), rather than a spin-Hall current (transverse).

Therefore, in a  $d_{x^2-y^2}$ -wave AM, the “steering” of electrons is spin-dependent. Even if an electric field is applied along the diagonals, the electrons are “pushed” toward the axes  $X$  and  $Y$  because of the warped shape of the energy bands. Consequently, electrical resistance will depend heavily on the direction of the current. See Figure 11 for a later FET proposal based in this AM feature.

Next we explain the implications of AM on conductivity anisotropy profiles. We compute the Drude weight  $D$  (at zero temperature) by integrating the squared group velocity over the Fermi surface (FS)

$$D_{ij}^s = \int_{BZ} \frac{d^2\mathbf{k}}{(2\pi)^2} v_s^i(\mathbf{k}) v_s^j(\mathbf{k}) \delta(E_s(\mathbf{k}) - E_F) = \oint_{FS} \frac{d\ell(\mathbf{k})}{(2\pi)^2 \hbar} \frac{v_s^i(\mathbf{k}) v_s^j(\mathbf{k})}{|\mathbf{v}_s(\mathbf{k})|}, \quad i, j = x, y, \quad (23)$$

where  $d\ell/(\hbar|\mathbf{v}|)$  is the local density of states for a specific segment  $d\ell$  of the Fermi surface. It arises as the Jacobian in the coordinate transformation  $d^2\mathbf{k} = dk_\perp d\ell = dE d\ell/(\hbar|\mathbf{v}|)$ , when you convert the integral over the full 2D area of the BZ into a 1D line integral along the FS. This quantity characterizes the coherent charge transport and allows us to estimate the conductivity  $\sigma_{ij}^s = e^2 \tau D_{ij}^s$ , with  $e$  the electron charge and  $\tau$  the scattering time. We will ignore the units and refer to  $D^s$  simply as the spin conductivity tensor  $\boldsymbol{\sigma}^s$  measuring the relationship between an applied electric field and the resulting spin-polarized flow. In Figure 6 we show the conductivity anisotropy profile as a polar plot of

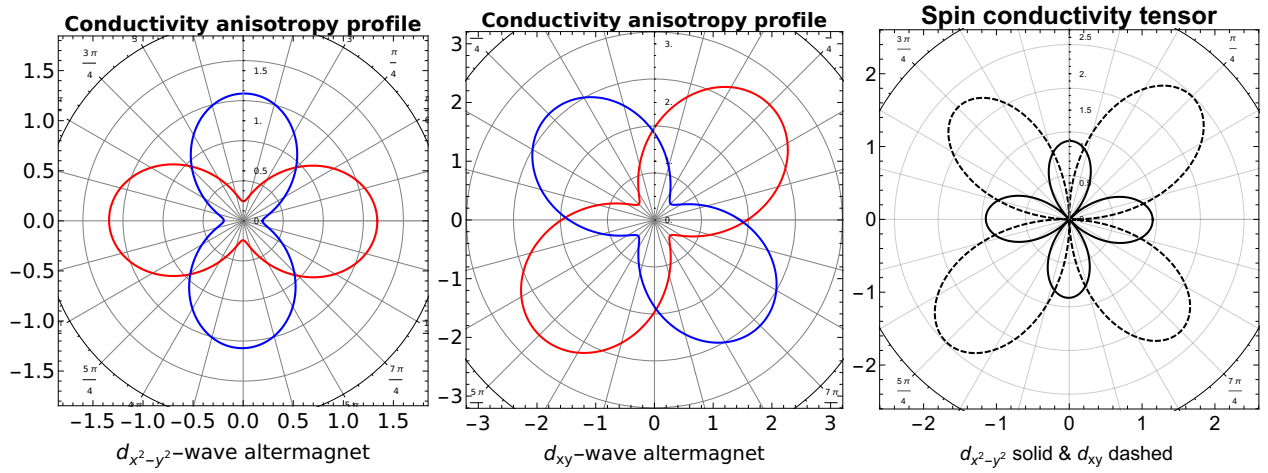


FIG. 6. Polar plot showing the conductivity's angular dependence for the  $d_{x^2-y^2}$ - and  $d_{xy}$ -wave ALMs. The anisotropic lobes correspond to the maximum group velocity directions. Hamiltonian parameters:  $J = 1, t = 1, t_a = 0.2$ .

$\sigma^s(\theta) = \mathbf{n}^T \boldsymbol{\sigma}^s \mathbf{n}$  as a function of the unit vector  $\mathbf{n} = (\cos \theta, \sin \theta)$  polar angle  $\theta$ . Fast electrons (high group velocity, see Figure 5) dictate the direction of maximum conductivity. While  $d_{x^2-y^2}$ -wave AM materials conduct current better along the principal axes,  $d_{xy}$ -wave AM materials conduct current well along diagonals. A transverse spin current is generated without any external magnetic field or relativistic spin-orbit coupling.

The quantity  $Q = \sigma^\uparrow - \sigma^\downarrow$  represents the spin conductivity tensor and is plotted in Figure 6, right panel. It is an important quantity of AM spintronic to quantify how much net spin is transported when we apply an electric field  $\mathbf{E}$ . The electric current for each spin channel is  $\mathbf{J}_s = \boldsymbol{\sigma}^s \mathbf{E}$ . The charge current (measured with an ammeter) is the sum  $\mathbf{J}_{\text{charge}} = \mathbf{J}_\uparrow + \mathbf{J}_\downarrow$ , whereas the spin current (the flow of angular momentum) is the difference  $\mathbf{J}_{\text{spin}} = \mathbf{J}_\uparrow - \mathbf{J}_\downarrow$ . Therefore, the conductivity tensor  $Q$  determines the material's ability to generate a spin current from a charge voltage. In a standard AFM, the two sublattices  $A$  and  $B$  are identical but inverted, so that symmetry dictates that  $Q = 0$ ; that is, both spins move at the same speed when we apply a voltage (there is no net flow of spin). However, in an AM material, although the magnetization remains zero as in the case of AFM, yet  $\sigma^\uparrow \neq \sigma^\downarrow$  in specific directions due to the group velocity mismatch. Consequently, if we construct a device using a  $d_{x^2-y^2}$ -wave AM and apply an electric field along the  $X$ -axis, we measure a current but, since spin up electrons are moving faster than spin down electrons, the current exiting the material is highly spin-polarized. As we have already commented in the Introduction, this also implies a SST that makes AM highly desirable as an alternative to more traditional SOT-MRAM (see [14] for recent progress), where a pure spin current is generated to flip a magnetic bit, without the need for the stray magnetic fields of a FM.

## V. REAL-SPACE NANORIBBON STRUCTURE ANALYSIS

We now turn into a real-space representation of our AM by performing an inverse Fourier transform. We study a 2D sample of area  $A = L_x L_y$  (a nanoribbon), so that our spin-up and spin-down Hamiltonian matrices are both of size  $D = 2A$  (remember that we are setting the lattice constant to  $a = 1 \text{ nm}$ ).

### A. Fidelity-susceptibility

The characterization of topological phases is usually done in momentum space through the Berry phase and Chern, winding, Pontryagin, etc., topological invariants, as we have seen in Section III. TPTs fall outside the Landau framework of QPTs (usually characterized by a spontaneous symmetry breaking) because the two topological phases can have exactly the same symmetry, although different topology. In addition, while QPTs are characterized by local order parameters (e.g. magnetization), for TPTs we have global topological invariants. However, QPTs and TPTs still share similarities. The effective AM strength represented in Figure 4 can be still seen as a kind of order parameter with lower values in the BI phase and higher values in the TI phase. Also, typical information theory markers of QPTs [like fidelity-susceptibility, entanglement entropy, delocalization measures, etc.] have also proven to be useful

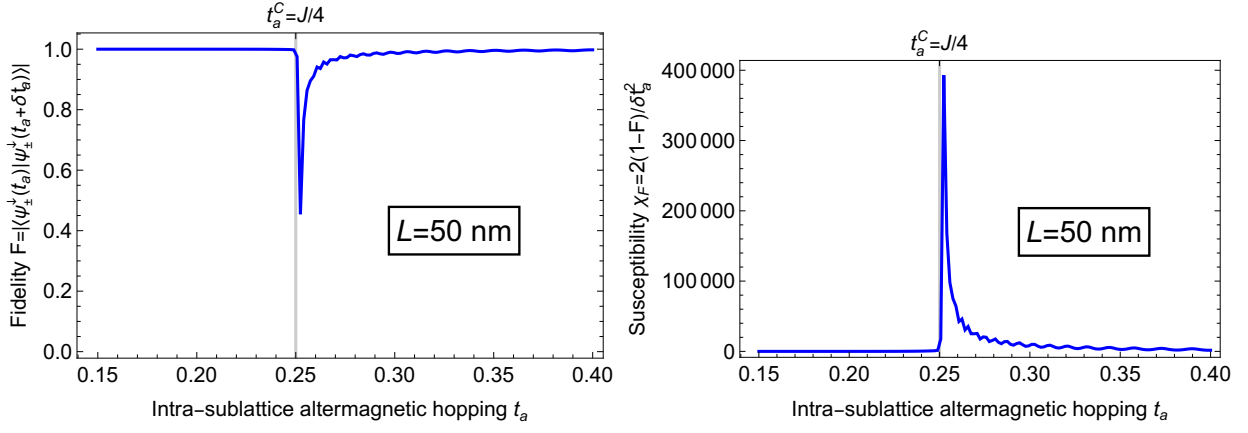


FIG. 7. Fidelity (left) and fidelity-susceptibility (right) of spin-down edge states as a function of  $t_a$  for a sample of size  $L_x = L_y = 50$  nm. Hamiltonian parameters:  $J = 1 = t \rightarrow t_a^C = J/4 = 0.25$ .

for characterizing TPTs; see e.g. [15–17] for Xenes, [18, 19] for phosphorene, [20–22] for HgTe/CdTe quantum wells and [23] for twisted bilayer graphene. Let us see how fidelity-susceptibility characterizes our TPT across the critical point  $t_a^C$ .

Just as the occurrence of QPTs is often marked by a sudden alteration in the structure of the ground-state wavefunction, the phenomenon of TPTs is also accompanied by an abrupt change in the structure of edge states  $\psi(t_a)$  at  $t_a = t_a^C$ . This change is captured by the fidelity [24, 25]

$$F(t_a, \delta t_a) = |\langle \psi(t_a) | \psi(t_a + \delta t_a) \rangle|, \quad (24)$$

which measures the similarity between two close states. Even more convenient is the fidelity-susceptibility

$$\chi_F(t_a) = - \left. \frac{\partial^2 F(t_a, \delta t_a)}{\partial(\delta t_a)^2} \right|_{\delta t_a=0} \approx 2 \frac{1 - F(t_a, \delta t_a)}{\delta t_a^2}, \quad \delta t_a \ll 1, \quad (25)$$

which is the leading term in the expansion of  $F$  in  $\delta t_a^2$  and has the advantage of reducing the dependence on the practical choice of  $\delta t_a$  with respect to  $F$ . The susceptibility  $\chi_F$  is also related to quantum Fisher information by  $\mathcal{F} = 4\chi_F$  and therefore to sensing precision to estimate  $t_a$  though the quantum Cramer-Rao bound  $\Delta t_a = 1/\sqrt{n\mathcal{F}(t_a)}$ , with  $n$  the number of measurement repetitions; this bound dictates the best possible precision allowed by quantum mechanics for estimating a parameter.

In Figure 7 we represent  $F$  and  $\chi_F$  for edge (near gap) states (either valence or conduction) as a function of  $t_a$  in a neighbourhood of the critical point  $t_a^C = J/4$  for  $L = 50$  nm ( $J = 1 = t$ ). An abrupt drop of fidelity and a snappish peak in susceptibility are clearly seen at  $t_a^C$ . Therefore, the sensing precision is highly enhanced at  $t_a^C$ . This provides an information-theoretic characterization of the TPT that is complementary to the Berry picture.

## B. Spatial texture and chirality

Let us now look at the real-space Hamiltonian wavefunctions segregation in a finite AM cluster. We will focus on bulk (highest energy level) and edge [energy floor for conduction “LUMO” and energy ceiling for valence “HOMO”] states.

In the momentum-space band structure, spin polarization is observed through energy splitting  $E_\uparrow(\mathbf{k}) \neq E_\downarrow(\mathbf{k})$  (in general). However, in real space, spin polarization becomes a spin density texture or chirality near boundaries or defects. The total set of energy levels is identical  $\{E_\uparrow\} = \{E_\downarrow\}$  but the wavefunctions are different:  $|\psi^\uparrow(x, y)|^2 \neq |\psi^\downarrow(x, y)|^2$ .

In Figure 8 we represent the spinor probability density, separated for the two components  $(\psi_A^s, \psi_B^s)$ , for spin up and down electrons. We have closed the valence band minimum and conduction band maximum energies (8) (referred to as bulk states  $|E| \gg 0$ , top panel in Figure 8) and the HOMO and LUMO energies (referred to as edge states  $|E| \sim 0$ , bottom panel in Figure 8). Bulk electrons are localized toward the center  $(x_c, y_c) = (L_x/2, L_y/2)$  of the sample, the probability distributions  $|\psi_\tau^\uparrow(x, y)|^2$  being sharper (more concentrated) at  $(x_c, y_c)$  in sublattice  $\tau = A$  (blue density

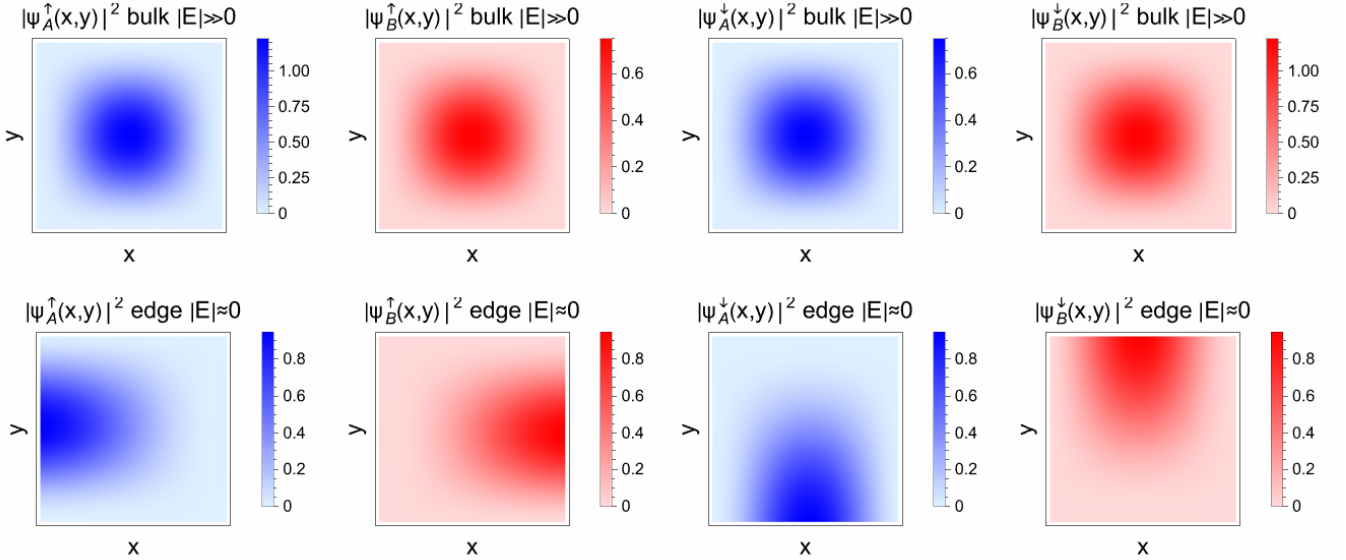


FIG. 8. Four-spinor probability density ( $|\psi_A^+|^2, |\psi_B^+|^2, |\psi_A^-|^2, |\psi_B^-|^2$ ) $_{\pm}$  as a function of  $(x, y) \in [0, 100] \times [0, 100]$  nm for bulk (top row) and edge (bottom row) Hamiltonian eigenstates. Densities were renormalized by  $L_x L_y$  to range from 0 to  $\sim 1$ . Hamiltonian parameters:  $J = 1, t = 1, t_a = J/4 = t_a^C$ .

plots) than in sublattice  $\tau = B$  (red density plots); the opposite occurs for spin  $\downarrow$ . In contrast, edge states are more concentrated at the sample boundaries. Since we know that spin up (down) electrons prefer to move along the  $X$  ( $Y$ ) direction, they will “pile up” differently when they hit the walls of the finite sample, resulting in a spin quadrupole pattern in real space. Indeed, spin  $\uparrow$  electrons pile up to the west of the sample at sublattice  $A$  and to the east at sublattice  $B$ , whereas spin  $\downarrow$  electrons accumulate to the south at sublattice  $A$  and to the north at sublattice  $B$ . For  $d_{xy}$ -wave AMs, probability density concentrates along diagonals,  $x = y$  for spin up and  $x = -y$  for spin down. Note that if the plot is rotated by  $90^\circ$ , red becomes blue, reflecting the  $d$ -wave symmetry.

### C. Global and local density of states

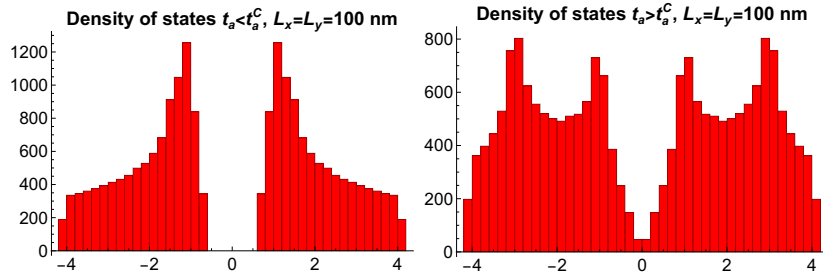


FIG. 9. DOS for spin up (similar results for spin down) in the BI ( $t_a = 0.1$ , left) and TI ( $t_a = 0.5$ , right) phases, for a sample of  $L_x = L_y = 100$  nm. Hamiltonian parameters:  $J = 1 = J$ .

A common characteristic of topological phases is the development of topological zero-energy (flat bands) edge states. This is an important phenomenon related to the appearance of van Hove singularities at zero energy, which contribute to the sharp peaks in the corresponding density of states (DOS) measured as follows

$$\text{DOS}_\eta(E) = \sum_{n=1}^D \delta_\eta(E - E_n), \quad (26)$$

where  $E_n$  are the Hamiltonian eigenvalues. Low-energy flat bands also develop at magic angles in twisted bilayer graphene [26]. This flattening of moiré bands at magic angles is accompanied by a vanishing of the effective Dirac-point Fermi velocity and strong enhancement of the counterflow conductivity, as experimentally measured by [27, 28]. Flat bands and magic angles are also captured by fidelity-susceptibility and other information entropy measures [23].

In Figure 9 we show the DOS for spin-up electrons (identical for spin-down electrons) below and above the critical point  $t_a^C$ . Indeed, flat bands (near zero-energy) develop above  $t_a^C$  but, in this case, the peaks are not quite sharp. The DOS also does not provide information on the spin-splitting effect, because up and down electron contributions are identical. Therefore, we resort to a more convenient/interesting magnitude, such as the Local Density of States (LDOS), which combines Hamiltonian eigenvalues and eigenvectors.

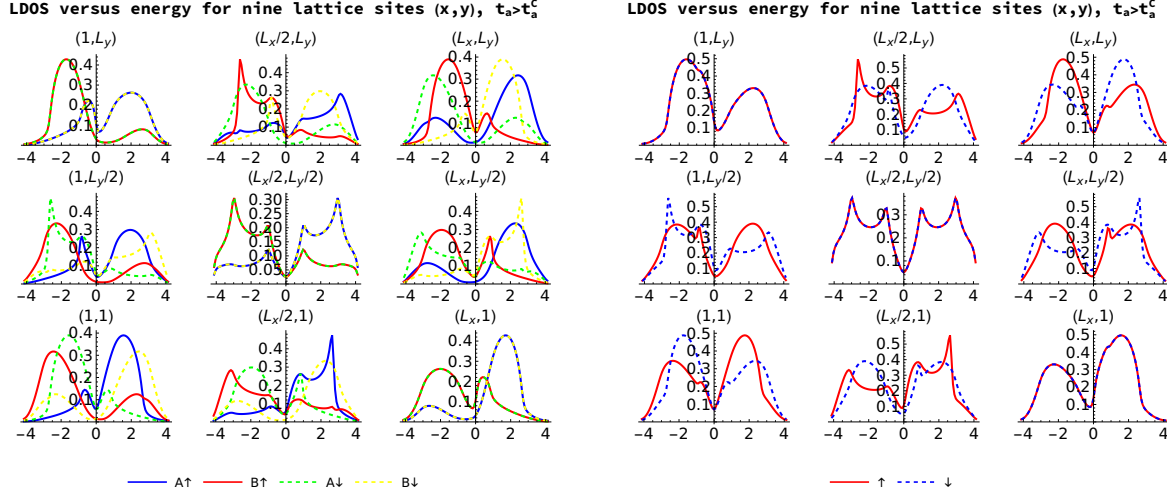


FIG. 10. LDOS as a function of the energy  $E$  for nine lattice sites  $(x, y)$  of our rectangular lattice: corners, midpoints sides and center. Left: resolved by sublattice and spin. Right: resolved by spin. Sample of  $L_x = L_y = 100$  nm. Hamiltonian parameters:  $t = 1.0$ ,  $J = 1.0$ ,  $t_a = 0.5$ .

To compute the LDOS, we evaluate how much of the total electronic density at a specific energy  $E$  is concentrated on a specific lattice site. The formula of LDOS at energy  $E$  on a lattice site  $(x, y)$  is

$$\text{LDOS}_{\eta}^{(x,y)}(E) = \sum_{n=1}^D |\psi_n(x, y)|^2 \delta_{\eta}(E - E_n) \quad (27)$$

where  $E_n$  and  $\psi_n$  are the eigenvalues and eigenvectors of our  $D = 4L_x L_y$  size (in lattice constant  $a = 1$  units) tight-binding matrix Hamiltonian. We want to separate the contributions to LDOS by sublattice  $\tau = A, B$  and spin  $s = \pm 1$ . In Figure 10 we plot the LDOS as a function of the energy  $E$  for nine lattice sites  $(x, y)$  of our rectangular lattice: corners, midpoints sides and center. The left panel is resolved by sublattice and spin, whereas the right panel is resolved just by spin (i.e., the combined  $A + B$  contributions).

Based on both LDOS plots provided, we draw some conclusions about our sample's physics. LDOS distinguishes lattice, spin, valence and conduction contributions at different edges and vertices. In general, the electronic density is more concentrated about the center of the valence and conduction bands, with a clear bias between the LDOS valence distribution ( $E < 0$ ) and the conduction distribution ( $E > 0$ ) at the different edges, but not at the center  $(L_x/2, L_y/2)$  of the sample, where both contributions are balanced. This means that the bulk states are spin-degenerate (or compensated); i.e., there is no net magnetization. Disregarding sublattice  $A, B$  (right panel), we can say that an electron moving in the bulk has an equal probability of being spin-up or spin-down (note that the red and blue curves overlap perfectly). This overlap also happens for electrons located about the anti-diagonal corners, but now there is a noticeable bias between valence and conduction. This corresponds to the PT symmetry,  $(x, y) \rightarrow -(x, y)$  and  $E \rightarrow -E$ , of our AM.

Note also that the spin-up conduction (valence) electronic density is more (less) concentrated downwards than upwards. The spin-down conduction (valence) electronic density is more (less) concentrated toward the right than toward the left. This picture is compatible with the conductivity profile of Figure 6. In fact, using a traffic analogy,  $X$ -axis is a highway for spin-up electrons, whereas they experience a traffic jam in the  $Y$ -direction. This creates piles of spin-up electrons at the bottom (for  $E > 0$ ) or at the top (for  $E < 0$ ). A similar reasoning applies to spin-down

electrons applying a 90° degrees rotation. We next discuss a split-drain FET architecture based in this AM singular characteristic.

#### D. Hybridization gap and FET proposal for nanoribbons

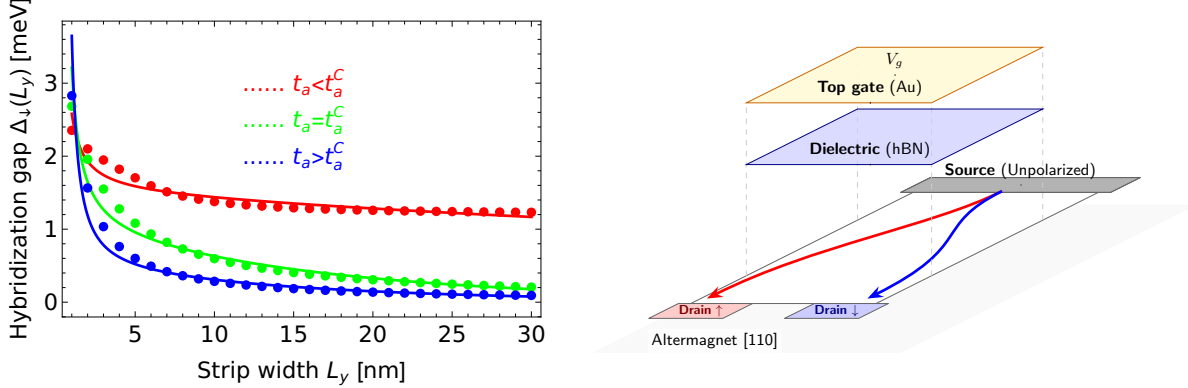


FIG. 11. Left panel: hybridization gap for spin-down electrons in a strip geometry of length  $L_x = 30$  nm as a function the strip width  $L_y$ , before, after and at the critical point  $t_a^C$ . Hamiltonian parameters:  $t = 1.0, J = 1.0 \Rightarrow t_a^C = 0.25$ . Right panel: Split-drain AM FET geometry.

Now we consider nanoribbons of size  $L_x L_y$  with  $L_x \gg L_y$ . Edge states in these nanoribbons usually display an exponential behavior,  $\psi(y) \sim \exp(-\kappa y)$ , to account for exponential localization at the boundaries  $y = 0, L_y$  (see e.g. [22, 29] for the case of HgTe quantum wells in an infinite strip of width  $L$ ). When the coherence length  $\lambda = 1/\text{Re}(\kappa)$  of edge states is comparable to the strip width  $L_y$ , states from opposite edges can overlap (tunneling between edges occurs), leading to a gap opening in the edge state spectrum that usually scales exponentially with the strip width, for large enough  $L_y$ . We propose a fitting for the hybridization gap of the following form

$$\Delta(L_y) = \Delta_0 e^{-L_y/\lambda + \xi/L_y}, \quad L_y \geq 1, \quad (28)$$

which accounts for values of  $L_y$  not necessarily large. In Figure 11 (left panel) we plot  $\Delta(L_y)$  as a function of the strip width  $L_y$ , for a fixed strip length of  $L_x = 30$  nm, and for three values of  $t_a$ : below, above and at the critical point  $t_a^C$ . We restrict ourselves to spin down electrons; the gap for spin-up electrons exhibits a similar behavior except for low  $L_y$ . The values of  $\Delta_0$ , the coherence length  $\lambda$  and the low  $L_y$  behavior captured by  $\xi$  are given in Table I. We also include the gap for the square sample ( $L_y = L_x$ ) in the last column. In general, the gap decreases with the ribbon width  $L_y$ , more drastically for narrow than for wide ribbons. In the topological phase  $t_a \geq t_a^C$ , the coherence length is  $\lambda \simeq 16$  nm. We see that, in fact, for values of  $L_y$  below  $\lambda$ , the gap is widening significantly, reaching characteristic values of  $\Delta \sim 1$  meV for ultra-narrow ribbons, likely  $L_y < 10$  nm, depending on the material's parameters (remember that we are using  $J = 1 = t$  meV).

$\Delta(L_y)$	$\Delta_0$ [meV]	$\lambda$ [nm]	$\xi$ [nm]	$\Delta(30)$ [meV]
$t_a = 0.1$ [meV]	1.48	117	0.56	1.23
$t_a = 0.25$ [meV]	1.01	17	1.22	0.21
$t_a = 0.5$ [meV]	0.47	16	2.12	0.09

TABLE I. Fitting parameter values of the hybridization gap (28) for spin-down electrons in a strip geometry of length  $L_x = 30$  nm. Hamiltonian parameters:  $t = 1.0, J = 1.0 \Rightarrow t_a^C = 0.25$ .

This noticeable and controllable variation in the gap, together with the spatial segregation and spin-splitting already commented, suggests the design of a novel device architecture: an AM FET in the topological phase. The split-drain FET geometry is sketched in Figure 11 (right panel). By aligning the transport channel (source-drain axis) along the  $[110]$  diagonal of the  $d_{x^2-y^2}$ -wave AM (or along the  $X$  axis of the  $d_{xy}$  configuration), the intrinsic group velocity mismatch steers spin- $\uparrow$  and spin- $\downarrow$  carriers toward opposite lateral boundaries. By designing the contacts to touch only one side of the ribbon, a pure spin current could be turned ON and OFF using the gate. This is the “Holy

Grail" of spintronics (see e.g. [30] for other recent "edgetronics" proposals in 2D AMs). For the transistor to work at temperature  $T$ , the finite-size gap must be larger than the thermal energy,  $\Delta(L_y) > k_B T$ , which is about 26 meV at room temperature. This should work in principle for ultra-narrow ribbons at liquid nitrogen temperatures. Higher temperatures could be allowed based on more realistic values of the staggered exchange potential or band splitting  $J \sim 50 - 500$  meV.

## VI. INFINITE STRIP GEOMETRY

First, we studied the band structure in momentum space and then the crystal structure in real space of our AM. Now we turn to a mixed momentum-real-space picture.

### A. Edge and bulk spectra

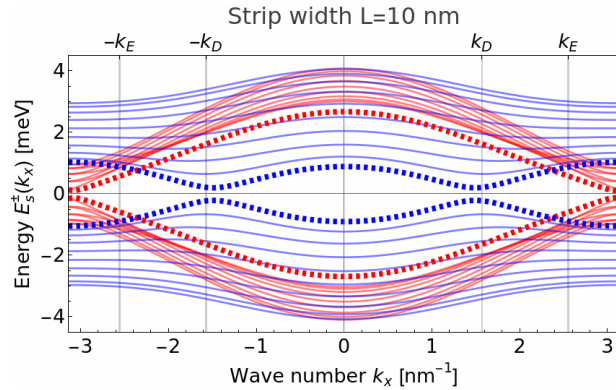


FIG. 12. Energy spectrum  $E_s^\pm(k_x)$  for  $L = 10$  nm and  $t_a > t_a^C$ . Bulk (solid) and edge (thick dashed) for spin-up (red) and spin-down (blue) Hamiltonian eigenstates. Material parameters  $J = 1, t = 1, t_a = J/2$ .

To investigate the edge states, we adopt a ribbon geometry of strip width  $L_y = L$ , infinite in  $x \in (-\infty, \infty)$  and finite in  $y \in [0, L]$ , with  $y_n = na$  and  $n = 0, \dots, N = L/a$  the site indices (remember that we are setting the lattice constant to  $a = 1$  nm for simplicity). Thus, we employ a mixed representation for our wavefunctions  $\psi(k_x, y)$ . We perform a partial Fourier transform in the spin- $s$  Hamiltonian  $\mathcal{H}_s = \int_{\text{BZ}} d\mathbf{k} c_{\mathbf{k}}^\dagger H_s(\mathbf{k}) c_{\mathbf{k}}$  by substituting the annihilation (viz. creation) operators

$$c_{\mathbf{k}} = \frac{1}{L} \sum_{n=0}^N e^{ik_y y_n} c_{k,n}, \quad y_n = na, \quad N = L/a, \quad (29)$$

to obtain the tight-binding Hamiltonian

$$\mathcal{H}_s = \sum_{k,n} \mathcal{E}_s(k) c_{k,n}^\dagger c_{k,n} + \mathcal{T} c_{k,n}^\dagger c_{k,n+1} + \mathcal{T}^\dagger c_{k,n+1}^\dagger c_{k,n}, \quad (30)$$

in the position (discrete)  $y = na$  and momentum  $k = k_x$  spaces. The  $2 \times 2$  matrix  $\mathcal{E}_s(k)$  results from eliminating all terms depending on  $k_y$  in  $H_s(\mathbf{k})$ . Those  $k_y$ -terms then contribute to the matrix  $\mathcal{T}$ . Doing so, we have

$$\mathcal{E}_s = \begin{pmatrix} sJ + 2t_a \cos(k_x) & t(1 + e^{-ik_x}) \\ t(1 + e^{ik_x}) & -sJ - 2t_a \cos(k_x) \end{pmatrix}, \quad \mathcal{T} = \begin{pmatrix} -t_a & 0 \\ t(1 + e^{ik_x}) & t_a \end{pmatrix}. \quad (31)$$

The Hamiltonian matrix  $\mathcal{H}_s$  is of size  $2N = 2L/a$  and is numerically diagonalized. Figure 12 shows the energy spectrum  $E_s(k_x)$  for a strip width of  $L = 10$  nm in the topological phase  $t_a > t_a^C$ , composed of both: bulk (solid) and edge (thick dashed) spin-up (red) and spin-down (blue) states. We observe some important differences with the infinite sample spectrum of Figure 3. Firstly, Dirac  $\pm k_D$  and up-down spin edge-state  $k_E$  crossing points are slightly shifted with respect to the  $L \rightarrow \infty$  case. We also observe the opening of the gap for finite  $L$  discussed in previous Section V D for finite size nanoribbons.

## B. Edge state structure

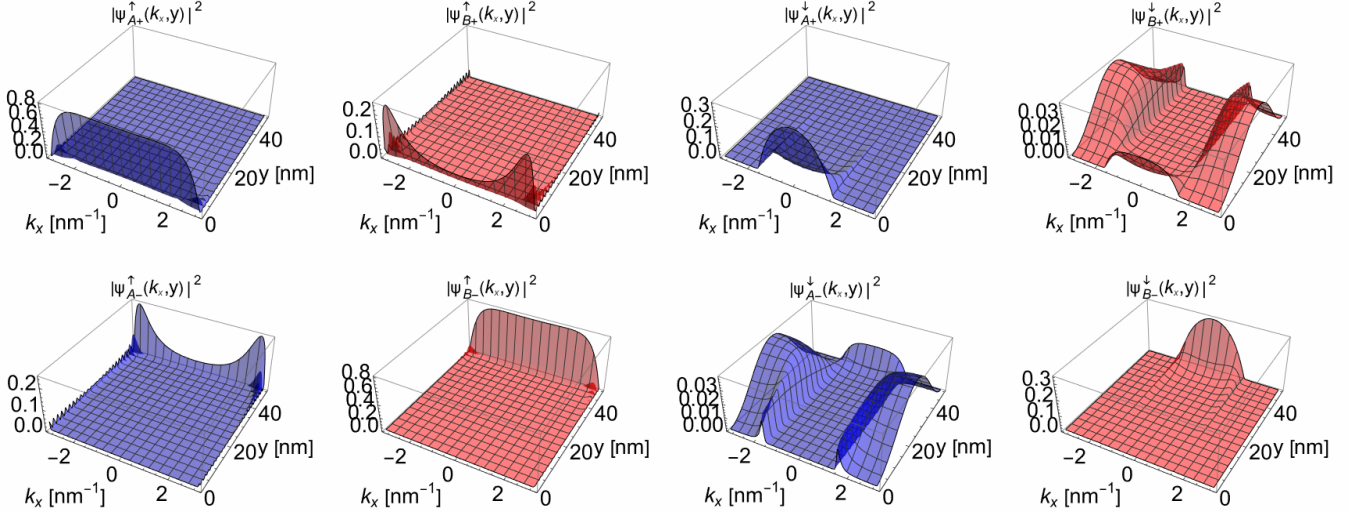


FIG. 13. Four spinor probability density ( $|\psi_A^\uparrow(k_x, y)|^2, |\psi_B^\uparrow(k_x, y)|^2, |\psi_A^\downarrow(k_x, y)|^2, |\psi_B^\downarrow(k_x, y)|^2$ )<sub>±</sub> as a function of  $(k_x, y)$  for conduction (+: top panel) and valence (-:bottom panel) edge staes. Strip width  $L = 50\text{ nm}$ . Hamiltonian parameters:  $J = 1, t = 1, t_a = J/2 > t_a^C$

We are interested in the particular structure of edge states in  $(k_x, y)$  space. Arranging our 4-spinor states as  $\{\psi_A^\uparrow, \psi_B^\uparrow, \psi_A^\downarrow, \psi_B^\downarrow\}$ , in Figure 13 we plot the probability densities  $|\psi_\tau^s(k_x, y)|^2$ , for the four components (separately), for conduction (top row) and valence (bottom row) edge states on a strip geometry of width  $L = 50\text{ nm}$ . Spin up conduction (valence) electrons are localized at the edge  $y = 0$  ( $y = L$ ). This is compatible with the “traffic analogy” given in Section V C, where we said that spin-up electrons experience a traffic jam in the  $Y$ -direction, remaining “parked” at  $y = 0, L$ . The structure for spin-down electrons is less straightforward to explain. For it, we shall use the “inverse participation ratio” as a measure of localization.

## C. Inverse participation ratio and edge localization

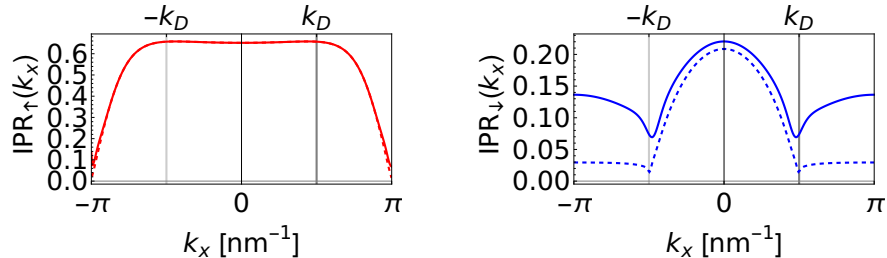


FIG. 14. IPR of spin-up (red) and spin-down (blue) edge conduction states for  $L = 10\text{ nm}$  (solid) and  $L = 50\text{ nm}$  (dashed). Hamiltonian parameters:  $J = 1, t = 1, t_a = J/2 > t_a^C$

In general, IPR measures the spreading of a vector’s expansion  $|\psi\rangle = \sum_{n=1}^N c_n |n\rangle$  in a given basis  $\{|n\rangle, n = 1, \dots, N\}$ . For a normalized vector  $|\psi\rangle$ , the probabilities  $p_n = |c_n|^2$  to find  $|\psi\rangle$  in  $|n\rangle$  fulfill  $\sum_{n=1}^N p_n = 1$ . The inverse participation ratio of  $\psi$  is then defined as follows  $\text{IPR}_\psi = \sum_{n=1}^N p_n^2 = \sum_{n=1}^N |c_n|^4$ . The smallest value  $\text{IPR}_\psi = 1/N$  corresponds to an equally weighted superposition  $|c_n| = 1/\sqrt{N}, \forall n$  (fully delocalized state), whereas the highest value  $\text{IPR}_\psi = 1$  corresponds to a perfectly localized state, that is,  $c_n = \delta_{n,n_0}$  for some  $n_0$ . The concept can be similarly extended

to the representation of the wavevectors in position, momentum, or other spaces, to study the vector's spreading or localization in the given space basis.

In our case, the IPR of a spin  $s$  2-spinor  $\psi^s = (\psi_A^\uparrow, \psi_B^\uparrow)$ , normalized as  $\int_0^L dy |\psi^s(k_x, y)|^2 = 1$ , in position  $y$  space for each value of the momentum  $k_x$  is given by

$$\text{IPR}_s(k_x) = \int_0^L dy |\psi^s(k_x, y)|^4, \quad (32)$$

where we understand  $|\psi^s|^4 = |\psi_A^s|^4 + |\psi_B^s|^4$ .

Figure 14 displays  $\text{IPR}_s(k_x)$  (valence and conduction coincide) for spin-up (red) and spin-down (blue) edge states for  $L = 10$  nm (solid) and  $L = 50$  nm (dashed). Edge states are more localized in space  $y \in [0, L]$  for low momentum  $|k_x| < k_D$ . Spin-down edge states become increasingly delocalized at the Dirac points, especially for larger strip widths  $L$ , where they delocalize (transmute to bulk states) for  $|k_x| > k_D$ . Spin-up electrons are highly localized in momentum space, except near  $k_x \simeq \pm\pi$ , where they delocalize (merge into the bulk).

## VII. COMMENTS AND CONCLUSIONS

The field of altermagnetism has rapidly transitioned from a theoretical curiosity to a cornerstone of modern condensed matter physics. Such a rapid shift may leave aspects of the theoretical foundation insufficiently examined or explained, motivating a deeper analysis. The literature is enormous (see e.g. [31, 32] for recent reviews), but it is sometimes too specialized, focusing more on the experimental aspect than on the theoretical one. This study aims to contribute to “filling this gap”.

We have seen that the AM undergoes a topological semimetal transition at the critical value  $t_a^C = J/4$  of the intra-sublattice AM hopping strength  $t_a$ . This is a transition from a gapped AM insulator to a gapless nodal AM (a semimetal with Dirac points). In the BI phase, the exchange splitting  $J$  is strong enough to keep the bands separated everywhere. The AM modulation is too weak to overcome the gap; thus, the system is an insulator (assuming half-filling). At the transition point ( $t_a = J/4$ ), the bands touch at a single point  $\mathbf{k}_D = (0, \pi)$  for spin up and  $\mathbf{k}_D = (\pi, 0)$  for spin down. In the TI phase, the modulation is strong enough to invert the bands. The band touching point splits into two Dirac nodes that move along the  $k_y = \pi$  ( $k_x = \pi$ ) line for spin down (up) as  $t_a$  increases. These nodes are topologically protected (they carry a Berry phase of  $\pi$ ).

We also studied the effective spin polarization. It is not just about having a different number of up and down spin states; rather, it is about the motion asymmetry. Although the energy is d-wave symmetric, the Fermi surface is d-wave distorted and, consequently, the group velocity is d-wave steered. For  $d_{x^2-y^2}$ -wave AMs, spin-up (down) electrons preferentially move along the horizontal (vertical) axis. This distinguishes AMs from FMs, where the spin current is usually longitudinal (i.e., parallel to the charge current). Therefore, AM materials act as a “spin pump” or as a “spin-filter”. We also calculated the effective AM strength  $P_{\text{eff}}$  quantifying how much “usable” spin is available for transport for a given  $t_a$ . For our Hamiltonian parameter choice, values of  $P_{\text{eff}} \simeq 80\%$  can be attained in the topological phase.

In a finite size  $L_x L_y$  nanoribbon (which is what we care about in technology), spin polarization manifests as spin accumulation at the boundaries. This is the origin of the spin-Hall effect in these materials and the hallmark of the spin-splitter effect (or crystal-Hall effect) in this specific geometry. The abrupt change in the structure of edge states at the critical point  $t_a^C$  is captured by fidelity-susceptibility, which is related to Fisher information and sensing precision though the quantum Cramer-Rao bound. This could have consequences in the design of quantum sensors of topological nature. Also, by exploiting the hybridization gap  $\Delta(L_y)$  for ultrathin ribbons, we have proposed a topological AM field-effect transistor device. Unlike conventional semiconductors, this device’s ON state relies on ballistic edge transport, minimizing scattering. Furthermore, due to the intrinsic spin-momentum locking of the AM edges, such a device would inherently function as a spin-valve, controlling spin-polarized currents via electrostatic gating, provided the ribbon width  $L_y$  is sufficiently small (smaller than the coherence length  $\lambda$  of edge states) to open a gap exceeding thermal broadening.

We also discussed the infinite strip geometry and analyzed the localization of edge states with the inverse participation ratio. This entropic measure indicates how delocalized the spin-up or spin-down electron is in real-space  $y$  for a given momentum  $k_x$ .

Our next step will be the inclusion of spin-orbit couplings and their influence on the topological behavior of AMs, opening up the possibility to other g-, i- or p-wave symmetries. This is left for future work.

## ACKNOWLEDGMENTS

I thank the Spanish Ministry of Science, Innovation and Universities through the project PID2022-138144NB-I00 and the Junta de Andalucía through the project FQM-420.

## REFERENCES

- [1] I. I. Mazin, Editorial: Altermagnetism—a new punch line of fundamental magnetism, *Phys. Rev. X* **12**, 040002 (2022).
- [2] L. Šmejkal, J. Sinova, and T. Jungwirth, Beyond conventional ferromagnetism and antiferromagnetism: A phase with nonrelativistic spin and crystal rotation symmetry, *Phys. Rev. X* **12**, 031042 (2022).
- [3] L. Šmejkal, J. Sinova, and T. Jungwirth, Emerging research landscape of altermagnetism, *Phys. Rev. X* **12**, 040501 (2022).
- [4] J. Krempaský, L. Šmejkal, S. W. D’Souza, M. Hajlaoui, G. Springholz, *et al.*, Altermagnetic lifting of Kramers spin degeneracy, *Nature* **626**, 517 (2024).
- [5] H. Schiff, A. Corticelli, A. Guerreiro, J. Romhányi, and P. McClarty, The crystallographic spin point groups and their representations, *SciPost Phys.* **18**, 109 (2025).
- [6] I. I. Mazin, Altermagnetism in MnTe: Origin, predicted manifestations, and routes to detwinning, *Phys. Rev. B* **107**, L100418 (2023).
- [7] W. Feng, X. Zhou, L. Šmejkal, L. Wu, Z. Zhu, H. Guo, and Y. Yao, An anomalous hall effect in altermagnetic ruthenium dioxide, *Nat. Electron.* **5**, 735 (2022).
- [8] O. Fedchenko, J. Minár, A. Akashdeep, S. W. D’Souza, *et al.*, Observation of time-reversal symmetry breaking in the band structure of altermagnetic RuO<sub>2</sub>, *Sci. Adv.* **10**, eadg4883 (2024).
- [9] A. Manchon and S. Zhang, Theory of nonequilibrium intrinsic spin torque in a single nanomagnet, *Phys. Rev. B* **78**, 212405 (2008).
- [10] I. M. Miron, K. Garello, G. Gaudin, P.-J. Zermatten, M. V. Costache, S. Auffret, S. Bandiera, B. Rodmacq, A. Schuhl, and P. Gambardella, Perpendicular switching of a single ferromagnetic layer induced by in-plane current injection, *Nature* **476**, 189 (2011).
- [11] L. Liu, C.-F. Pai, Y. Li, H. W. Tseng, D. C. Ralph, and R. A. Buhrman, Spin-torque switching with the giant spin Hall effect of tantalum, *Science* **336**, 555–558 (2012).
- [12] R. González-Hernández, L. Šmejkal, K. Výborný, Y. Yahagi, J. Sinova, T. c. v. Jungwirth, and J. Železný, Efficient electrical spin splitter based on nonrelativistic collinear antiferromagnetism, *Phys. Rev. Lett.* **126**, 127701 (2021).
- [13] H. Bai, L. Han, X. Feng, Y. J. Zhou, R. Su, Q. Wang, L. Liao, W. Zhu, X. Chen, F. Pan, X. Fan, and C. Song, Observation of spin splitting torque in a collinear antiferromagnet RuO<sub>2</sub>, *Phys. Rev. Lett.* **128** 19, 197202 (2021).
- [14] V. D. Nguyen, S. Rao, K. Wostyn, and S. Couet, Recent progress in spin-orbit torque magnetic random-access memory, *npj Spintronics* **2**, 48 (2024).
- [15] M. Calixto and E. Romera, Identifying topological-band insulator transitions in silicene and other 2D gapped dirac materials by means of Rényi-Wehrl entropy, *EPL (Europhysics Letters)* **109**, 40003 (2015).
- [16] E. Romera and M. Calixto, Uncertainty relations and topological-band insulator transitions in 2D gapped dirac materials, *Journal of Physics: Condensed Matter* **27**, 175003 (2015).
- [17] M. Calixto and E. Romera, Inverse participation ratio and localization in topological insulator phase transitions, *Journal of Statistical Mechanics: Theory and Experiment* **2015**, P06029 (2015).
- [18] M. Calixto, E. Romera, and O. Castaños, Analogies between the topological insulator phase of 2D Dirac materials and the superradiant phase of atom-field systems, *International Journal of Quantum Chemistry* **121**, e26464 (2021).
- [19] O. Castaños, E. Romera, and M. Calixto, Information theoretic analysis of landau levels in monolayer phosphorene under magnetic and electric fields, *Materials Research Express* **6**, 106316 (2019).
- [20] M. Calixto, N. A. Cordero, E. Romera, and O. Castaños, Signatures of topological phase transitions in higher Landau levels of HgTe/CdTe quantum wells from an information theory perspective, *Physica A: Statistical Mechanics and its Applications* **605**, 128057 (2022).
- [21] M. Calixto, A. Mayorgas, N. A. Cordero, E. Romera, and O. Castaños, Faraday rotation and transmittance as markers of topological phase transitions in 2d materials, *SciPost Phys.* **16**, 077 (2024).
- [22] M. Calixto and O. Castaños, Localization and entanglement characterization of edge states in HgTe quantum wells in a finite strip geometry, *International Journal of Modern Physics B* **39**, 2550263 (2025).
- [23] M. Calixto, A. Mayorgas, and O. Castaños, Capturing magic angles in twisted bilayer graphene from information theory markers, *Physica E: Low-dimensional Systems and Nanostructures* **169**, 116199 (2025).
- [24] S.-J. Gu, Fidelity approach to quantum phase transitions, *International Journal of Modern Physics B* **24**, 4371–4458 (2010).
- [25] P. Zanardi and N. Paunković, Ground state overlap and quantum phase transitions, *Phys. Rev. E* **74**, 031123 (2006).
- [26] R. Bistritzer and A. H. MacDonald, Moiré bands in twisted double-layer graphene, *Proceedings of the National Academy of Sciences* **108**, 12233–12237 (2011).
- [27] Y. Cao, V. Fatemi, A. Demir, S. Fang, S. L. Tomarken, J. Y. Luo, J. D. Sanchez-Yamagishi, K. Watanabe, T. Taniguchi, E. Kaxiras, R. C. Ashoori, and P. Jarillo-Herrero, Correlated insulator behaviour at half-filling in magic-angle graphene superlattices, *Nature* **556**, 80–84 (2018).
- [28] Y. Cao, V. Fatemi, S. Fang, K. Watanabe, T. Taniguchi, E. Kaxiras, and P. Jarillo-Herrero, Unconventional superconductivity in magic-angle graphene superlattices, *Nature* **556**, 43–50 (2018).

- [29] B. Zhou, H.-Z. Lu, R.-L. Chu, S.-Q. Shen, and Q. Niu, Finite size effects on helical edge states in a quantum spin-hall system, *Phys. Rev. Lett.* **101**, 246807 (2008).
- [30] S. Fang, Z. Yang, J. Wang, X. Yang, J. Lu, C. H. Lee, X. Wang, and Y. S. Ang, Edgetronics in two-dimensional altermagnets (2025), [arXiv:2508.10451 \[cond-mat.mes-hall\]](https://arxiv.org/abs/2508.10451).
- [31] T. Jungwirth, R. M. Fernandes, E. Fradkin, A. H. MacDonald, J. Sinova, and L. Šmejkal, Altermagnetism: An unconventional spin-ordered phase of matter, *Newton* **1**, 100162 (2025).
- [32] Y. Fukaya, B. Lu, K. Yada, Y. Tanaka, and J. Cayao, Superconducting phenomena in systems with unconventional magnets, *Journal of Physics: Condensed Matter* **37**, 313003 (2025).